PLOS COMPUTATIONAL BIOLOGY

RESEARCH ARTICLE

Three-dimensional topology optimization model to simulate the external shapes of bone

Misaki Sakashita[1¤]*, Shintaro Yamasaki[2], Kentaro Yaji[2], Atsushi Kawamoto[3], Shigeru Kondo[1]

1 Graduate School of Frontier Biosciences, Osaka University, Suita, Japan, **2** Graduate School of Engineering, Osaka University, Suita, Japan, **3** Toyota Central R&D Labs., Inc., Nagakute, Japan

¤ Current address: Department of Applied Biological Science, Tokyo University of Science, Noda, Japan
* sakashitamsk@gmail.com

OPEN ACCESS

Citation: Sakashita M, Yamasaki S, Yaji K, Kawamoto A, Kondo S (2021) Three-dimensional topology optimization model to simulate the external shapes of bone. PLoS Comput Biol 17(6): e1009043. https://doi.org/10.1371/journal.pcbi.1009043

Editor: Philip K. Maini, Oxford, UNITED KINGDOM

Received: December 16, 2020

Accepted: May 5, 2021

Published: June 16, 2021

Data Availability Statement: All relevant data are within the manuscript and its Supporting information files.

Funding: This work was supported by the Japan Society for the Promotion of Science (JSPS, https://www.jsps.go.jp/english/) fellowship (19J11643 to M.S.) and funding from the Core Research for Evolutional Science and Technology (CREST, https://www.jst.go.jp/kisoken/crest/en/) of the Japan Science and Technology Agency (JST) (JPMJCR12W5 to S.K.). The funders had no role in

Abstract

Elucidation of the mechanism by which the shape of bones is formed is essential for understanding vertebrate development. Bones support the body of vertebrates by withstanding external loads, such as those imposed by gravity and muscle tension. Many studies have reported that bone formation varies in response to external loads. An increased external load induces bone synthesis, whereas a decreased external load induces bone resorption. This relationship led to the hypothesis that bone shape adapts to external load. In fact, by simulating this relationship through topology optimization, the internal trabecular structure of bones can be successfully reproduced, thereby facilitating the study of bone diseases. In contrast, there have been few attempts to simulate the external structure of bones, which determines vertebrate morphology. However, the external shape of bones may be reproduced through topology optimization because cells of the same type form both the internal and external structures of bones. Here, we constructed a three-dimensional topology optimization model to attempt the reproduction of the external shape of teleost vertebrae. In teleosts, the internal structure of the vertebral bodies is invariable, exhibiting an hourglass shape, whereas the lateral structure supporting the internal structure differs among species. Based on the anatomical observations, we applied different external loads to the hourglass-shaped part. The simulations produced a variety of three-dimensional structures, some of which exhibited several structural features similar to those of actual teleost vertebrae. In addition, by adjusting the geometric parameters, such as the width of the hourglass shape, we reproduced the variation in the teleost vertebrae shapes. These results suggest that a simulation using topology optimization can successfully reproduce the external shapes of teleost vertebrae. By applying our topology optimization model to various bones of vertebrates, we can understand how the external shape of bones adapts to external loads.

study design, data collection and analysis, decision to publish, or preparation of the manuscript.

Competing interests: The authors have declared that no competing interests exist.

Author summary

In this paper, we developed a computational method to investigate the relationship between three-dimensional bone shape and external loads imposed on bones. Many studies report that bone formation varies in response to external loads. An increased external load induces bone synthesis, whereas a decreased external load induces bone resorption. This relationship led to the hypothesis that the shape of bones adapts to external load. However, it remains unclear whether this hypothesis can explain the shape of bones. Here, we constructed a three-dimensional mathematical model that imitates the cellular activities of bone formation to attempt the reproduction of the shape of teleost vertebrae. In teleosts, the shape of the vertebrae differs among the species. We set the multiple types of external load conditions in the simulations and compared the simulation results with different teleost vertebrae. The produced structures that can resist the deformation of the surrounding tissues exhibited multiple structural features similar to the vertebrae of several teleost species. This result shows that the formation of bone shape can be explained by the adaptation to external load.

Introduction

Elucidating how the shape of bones is formed is essential to obtain an in-depth understanding of vertebrate development, as the body shape of vertebrates depends on a skeleton that is composed of differently shaped bones. To maintain the body shape of vertebrates, bones must be able to withstand various continual external loads, such as those imposed by gravity and muscle tension. Previous studies have demonstrated that a change in these external loads causes a morphological change in bones. For instance, femur bones become thinner and sparser in the zero-gravity environment of space flight [1, 2]. In addition, immobility due to a spinal cord injury changes the cross-sectional tibial geometry from the typical teardrop appearance to a more circular shape [3], and a bipedal goat without forelegs exhibits a narrowing of the pelvis relative to that of quadrupedal goats [4]. These findings suggest that unlike the shape of organs that is mainly determined genetically, bone shape is influenced by the external loads.

Indeed, this possibility has been supported by cytological studies showing that the cellular activities involved in bone formation are controlled by external loads. The main types of cells involved in bone shape are osteoblasts and osteoclasts. Osteoblasts secrete and mineralize the bone matrix, whereas osteoclasts break down and resorb the bones. These opposing activities of osteoblasts and osteoclasts vary according to the external load condition through osteocytic or non-osteocytic regulation mechanisms [5–10]; an increased external load induces bone synthesis [11], whereas a decreased external load induces bone resorption [12, 13]. These findings support Roux's paradigm that local cellular activities induced by external loads form bone shape [14–17] (sometimes this paradigm is integrated with other paradigm known as "Wolff's law" [16, 18, 19]).

To confirm this paradigm, computer simulations of the cellular activities in bone formation have been performed. In the field of biomechanics, Huiskes and colleagues developed a bone remodeling algorithm in which bone density is regulated by the strain energy density [20–23]. In this bone remodeling algorithm, bone addition occurs in high-strain-energy density areas and bone removal occurs in low-strain-energy density areas, thereby imitating the activities of osteoblasts and osteoclasts that are regulated according to external loads. Accordingly, this algorithm could produce the pillar structure aligned to the direction of external loads, which is the characteristic of the bone internal structure formed by trabeculae [23, 24]. In the same

period, many researchers have applied structural optimization methods to reproduce bone shape from an engineering perspective [25, 26]. One of the most widely utilized methods for this purpose is topology optimization [27–33]. Topology optimization optimizes the distribution of a material's density according to a physical quantity such as strain and stress, and has been used to generate the optimal shapes of different types of structures, such as machine parts and architecture [34, 35]. Although topology optimization was initially developed for purposes not related to imitating the bone formation process, the fundamental of its algorithm is the same as the bone remodeling algorithm [36]. In stiffness maximization, the addition and removal of a material occur according to the strain energy density, effectively reproducing the internal structure of the bone. These computer simulations in the different fields have explained that the internal structure of the bone adapts to the external loads, thereby facilitating research on abnormal bone shapes due to diseases [37, 38].

In contrast to the extensive simulations of bone internal structures, few computer simulations have been performed to reproduce the external shape formed by the cortical bones. However, because both the internal and external structures of bones are formed by osteoblasts and osteoclasts, it is reasonable to hypothesize that the bone's external shape can also be reproduced through the computer simulations. Based on this hypothesis, several researchers have attempted to reproduce the outline of the femur, tibia, and vertebrae as cross-sections [39–42]. Additionally, Mittag et al. [43, 44] produced three-dimensional (3D) tube-like structures to reproduce the external shape of the long bone shafts. However, actual bones exhibit 3D external shapes with a complex curved surface, which are difficult to represent with a cross-section or a simple geometric shape. Therefore, the aforementioned hypothesis remains to be examined. For this reason, we aimed to reproduce the 3D external shapes of bones. As topology optimization can be used to generate a variety of 3D structures, we considered that this approach would be suitable for simulating the 3D external shapes of bones. Furthermore, topology optimization can produce an optimal structure for multiple objectives, allowing for further modification of the simulation model. Hence, we used the stiffness maximization algorithm with topology optimization for the reproduction of external bone shapes.

In this study, we selected the teleost vertebrae as the subject for the simulation based on two advantageous characteristics. First, the skeleton of fish does not need to counteract gravity, unlike the case for terrestrial vertebrates. For this reason, the external load condition of teleost vertebrae is relatively simple. In a simulation, it is important to first set the load cases that define the type of external load that is applied to the bone, because the optimization process depends on the strain energy density caused by the load cases. As it is nearly impossible to directly examine the external load condition of bones, we need to try numerous optimizations for different load cases to reproduce the external shape of bones. Using teleost vertebrae allows us to apply this approach, as we can simply set the load cases. Second, the external shape of teleost vertebral bodies greatly varies among species. The vertebral bodies of teleost fish are mainly formed by the internal autocentrum and external arcocentrum, each with a distinct composition [45]. The internal autocentrum has an amphicoelous hourglass shape, which is invariable among species [46, 47] (Fig 1A). In contrast, the lateral structure of the vertebral bodies formed by the external arcocentrum varies among species [46–49] (Fig 1). This variation can be compared to the multiple 3D structures that are produced by optimizations for different load cases.

Here, we constructed a topology optimization model to attempt the reproduction of the lateral structures of teleost vertebral bodies. Because the external loads on teleost vertebrae arise from the deformation of the surrounding tissues [50, 51], we set multiple load cases based on anatomical studies and produced various types of structures. By comparing the optimization

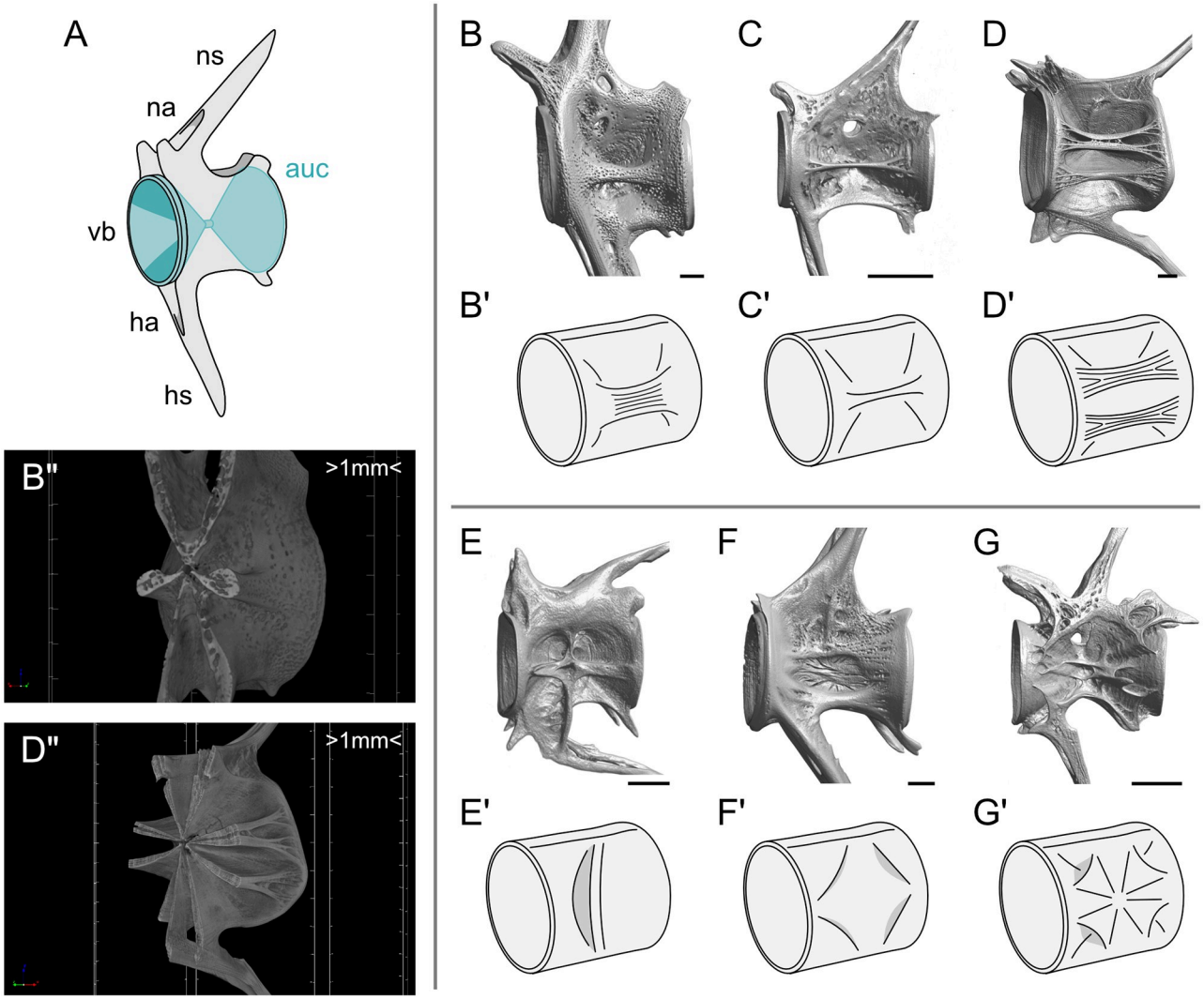

Fig 1. Anatomy of fish vertebrae. (A) Structure of the fish vertebrae. Abbreviations: auc: autocentrum; ns: neural spine; na: neural arch; vb: vertebral body; ha: hemal arch; hs: hemal spine. (B–G) Volume-rendered micro-computed tomography (micro-CT) images of left lateral views of the caudal vertebral bodies of (B) *Pagrus major*, (C) *Acropoma hanedai*, (D) *Zenopsis nebulosa*, (E) *Muraenesox cinereus*, (F) *Scarus forsteni*, and (G) *Macroramphosus sagifue*. (B'–G') Schematic illustrations of the morphological features of (B–G) that displays (B) a single thick longitudinal plate-like ridge (thick trabecula), (C) a single thin longitudinal plate-like ridge, (D) two longitudinal plate-like ridges, (E) a transverse plate-like ridge, (F) hump-like structures rising on the edge of the vertebral body, (G) tarp-like triangle ridges extending from the center to the edge of the vertebral body. (B" and D") Transverse sections at the midpoint of the vertebral bodies of (B") *P. major* and (D") *Z. nebulosa*. These images indicate that the lateral ridges extend from the vertebral body center. Scale bars: (B–F) 1 mm, and (G) 500 μm. In (B" and D"), the interval between scale markers is 1 mm.

https://doi.org/10.1371/journal.pcbi.1009043.g001

results to the teleost vertebrae, we examined whether the external shape of the teleost vertebrae can be reproduced using topology optimization.

Mathematical modeling

Topology optimization

In our topology optimization model, vertebral morphology is visualized as the distribution of the material density at each location $\rho(\mathbf{x})$ of an analysis domain. $\mathbf{x}$ indicates a position in the analysis domain and $\rho(\mathbf{x}) \in [0, 1]$ is a continuous and relative density. $\rho = 0$ indicates that the region is void and $\rho = 1$ indicates that the region is full of material. To obtain the distribution

of $\rho(\mathbf{x})$, we solved the following stiffness maximization problem with the assumption of static, linear elastic behavior:

$$\begin{aligned} \underset{\rho(\mathbf{x})}{\text{minimize}} \quad & f(\rho) \equiv \int_{\Gamma_t} \mathbf{t} \cdot \mathbf{u}\, d\Gamma \\ \text{subject to} \quad & g(\rho) \equiv \int_{\Omega} \rho\, d\Omega - V_f \int_{\Omega} d\Omega \leq 0. \end{aligned} \tag{1}$$

The objective function $f(\rho)$ represents the compliance, which is the work done by the external forces and is inversely proportional to the structural stiffness. Furthermore, $\mathbf{t}$ is the load vector, $\mathbf{u}$ is the displacement vector, and Γ is the boundary of the analysis domain Ω, where Γ_t in particular is where the load is applied. The constraint function $g(\rho)$ limits the amount of available material, and V_f is the volume fraction of the available material.

We obtained the displacement $\mathbf{u}$ by solving the following governing equations:

$$\left.\begin{aligned} -\nabla \cdot (\mathbf{E} : \boldsymbol{\epsilon}(\mathbf{u})) &= \mathbf{0} && \text{in} \quad \Omega \\ \mathbf{u} &= \mathbf{0} && \text{on} \quad \Gamma_u \\ (\mathbf{E} : \boldsymbol{\epsilon}(\mathbf{u})) \cdot \mathbf{n} &= \mathbf{t} && \text{on} \quad \Gamma_t \end{aligned}\right\}. \tag{2}$$

In the above, $\boldsymbol{\epsilon}$ is the strain tensor $\boldsymbol{\epsilon}(\mathbf{u}) = \frac{1}{2}(\nabla \mathbf{u} + \nabla \mathbf{u}^{\top})$ and Γ_u is the fixed boundary where the displacement is constrained. The linear elastic tensor $\mathbf{E}$ is expressed as $\mathbf{E} = \rho^P \mathbf{E}_0$ by the solid isotropic material with penalization method [35]. Furthermore, $\mathbf{E}_0$ is the elastic tensor of the material. The Young's modulus of the material is 20 GPa and the Poisson's ratio is 0.3, with reference to the values of zebrafish vertebrae [10, 52, 53]. The positive parameter $P \geq 1$ enforces the final designs with $\rho(\mathbf{x})$ at each location being either 0 or 1 through penalization of the stiffness for intermediate densities. In this study, $P = 3$ following [54].

We used the topology optimization method with a time-dependent equation developed by Kawamoto et al. [55] to solve this stiffness maximization problem, because this method is easy to implement using the commercial software COMSOL Multiphysics (we used version 5.4). The details of the equations and parameters are described in S1 Text. For the optimization of multiple load cases, the objective function $f(\rho)$ was defined with the compliances provided by the different load cases $f_i(\rho)$ ($i = 1, 2, \ldots, N$):

$$f(\rho) \equiv \sum_{i}^{N} \frac{1}{N} f_i(\rho) = \sum_{i}^{N} \frac{1}{N} \int_{\Gamma_{t_i}} \mathbf{t}_i \cdot \mathbf{u}_i\, d\Gamma, \tag{3}$$

where N denotes the number of load cases. In this study, we used Eq 3 for the optimizations for bending, shear, and torsional loads.

The optimizations in this paper can be reproduced by running S1 Code in LiveLink for MATLAB (we used MATLAB R2018b).

Analysis domain

The analysis domain of our topology optimization model could be divided into the internal and external domains, corresponding to the autocentrum and arcocentrum of teleost vertebral bodies (Fig 2). The internal domain had an amphicoelous hourglass shape, which imitates the autocentrum (Fig 2A). The geometry was defined by the parameters C_R, C_T, C_X, L, and θ (Fig 2B). We set the thickness of the hourglass-shaped domain to be small, because the thickness of the autocentrum is very thin in the adult stage. Also, as the angle of conical part of teleost

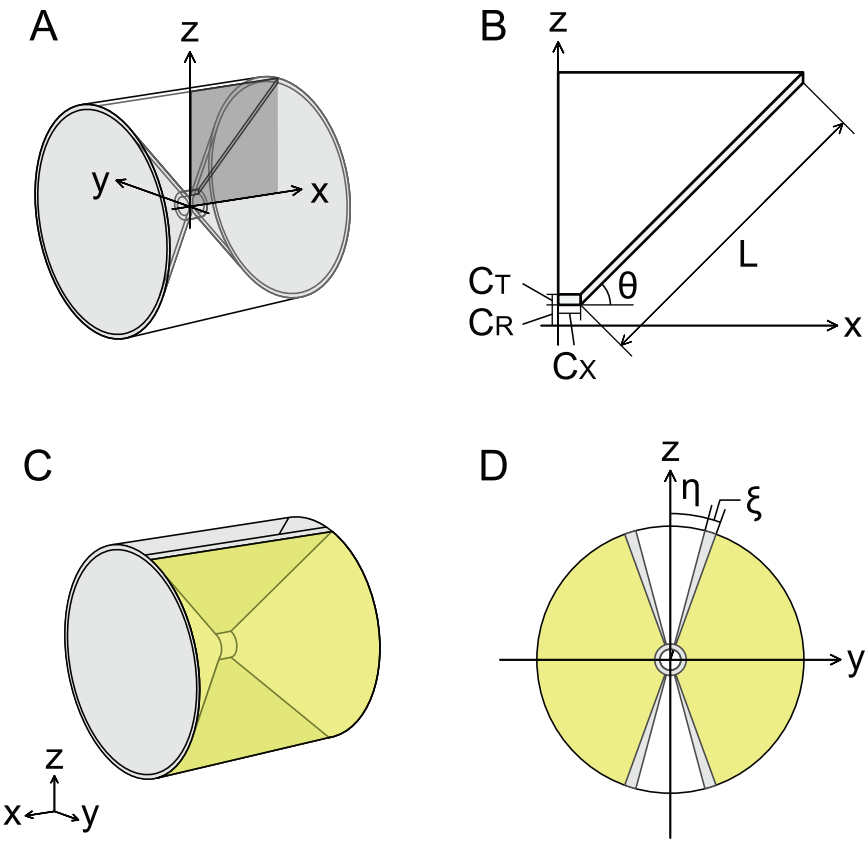

Fig 2. Simulation model. (A) Transparent view of entire structure. The light gray domain corresponds to the autocentrum. (B) Quarter cross-section of analysis domain on zx plane (dark gray plane in (A)). (C) Entire structure. The yellow-colored area is the design domain. (D) Transverse section at midpoint of analysis domain. The light gray wedge-shaped regions represent the vertebral arches. The geometric parameters are described in Table 1.

https://doi.org/10.1371/journal.pcbi.1009043.g002

vertebrae ranges approximately from 50˚ to 90˚ in many species (S1 Data and S1 Fig), we set the half angle of conical part θ to 45˚. Because the hourglass-shaped autocentrum and its formation are invariable among teleost species [46, 47, 56], we set the density $\rho = 1$ in the internal domain. Moreover, vertebral arches are formed separately from vertebral bodies during the early developmental stage, which is long before the lateral structure of the vertebral bodies is formed, and are later fused to the vertebral bodies [57, 58]. Based on this process, we set $\rho = 1$ in the domain of the vertebral arches and $\rho = d$ in the gap of these (Fig 2C and 2D). In this case, d is a very small positive approximate value of 0 (see S1 Text), and in this study, $d = 0.01$. The half gap width η of vertebral arches was set to 15˚ because the gap width range was approximately 30˚ to 60˚ in many species (S1 Data and S2 Fig). The remaining domain (yellow color in Fig 2) was the design domain in which the distribution of ρ was optimized. The geometric parameters are described in Table 1. The analysis domain size was set to approximately 1 cm^3 considering the size of teleost vertebral bodies.

The initial density value in the design domain was $\rho = d$. Therefore, the material was added at the beginning of the optimization process and was removed when the material volume exceeded the upper bound V_f (S1 Video). In this study, the difference in the initial density values did not influence the optimization results (See S1 Text and S3 Fig).

The optimized structure was displayed with isosurfaces of $\rho = 0.5$.

Table 1. Parameter settings to define geometry of analysis domain in Figs 2–6.

Parameter	Symbol	Value
Radius of cylindrical part (chordacentrum)	C_R	0.04 cm
Thickness of autocentrum	C_T	0.02 cm
Length of cylindrical part (chordacentrum)	C_X	0.04 cm
Length of conical part	L	0.6 cm
Half angle of conical part	θ	45˚
Width of vertebral arches	ξ	5˚
Half width of gap of vertebral arches	η	15˚

https://doi.org/10.1371/journal.pcbi.1009043.t001

Load cases

Since fish float in water, the effect of gravity on the teleost vertebrae can be considered to be minimal compared to that on terrestrial vertebrates. Indeed, the vertebrae of the space-flight medaka did not show significant changes in shape and bone mineral density [59]. In addition, a study using an amphibious fish species showed that the bone stiffness of the fish in water was lower than that of the terrestrially acclimated fish, and was comparable to that of fish under simulated microgravity using a random positioning machine [60]. Hence, in this study, we focused on the external loads occurring by deformation of the surrounding tissues. For instance, the lateral muscles are attached to the vertebrae, and the contraction of these muscles for axial body undulation exerts the external load on teleost vertebrae [50, 51]. Also, the intervertebral region between vertebral bodies contains bicone-shaped vacuolated notochord cells [61, 62] and the vertebral bodies are connected on the edges with collagen fiber bundles [63]. Based on these findings, we hypothesized that compressive and bending loads occur on autocentrum. Therefore, we applied compressive and bending loads in multiple directions to the concave surface and edge of the autocentrum (Figs 3 and 4). We also applied shear and torsional loads for the comparison of optimization results (Fig 5).

Moreover, as the lateral muscle is attached to the vertebral arches as well as vertebral bodies [51], we assumed that tensile loads to the vertebral arches occurred during body undulation. We applied the tensile loads in the left–right and dorsal–ventral axis directions to the vertebral arches (Fig 6).

The magnitude of each load F was 10^6 N/m^2 according to the mechanical analyses of teleost bones [64, 65]. In all load cases, we constrained the displacement to avoid the rigid body mode. Furthermore, we imposed the symmetric boundary condition. In the following descriptions, the position vector is $\mathbf{r} = (x, y, z)$, with $\mathbf{x} = (x, 0, 0)$, $\mathbf{y} = (0, y, 0)$, and $\mathbf{z} = (0, 0, z)$. Moreover, $\mathbf{n}$ is the normal vector.

The nine types of load cases we attempted were described below:

Compressive load in normal direction. A compressive load in the normal direction $\mathbf{t} = -F\mathbf{n}$ was applied to the concave surface of the hourglass-shaped domain (Fig 3).

Compressive load in horizontal direction. A compressive load in the horizontal direction $\mathbf{t} = -F\frac{\mathbf{x}}{|\mathbf{x}|}$ was applied to the concave surface of the hourglass-shaped domain (Fig 3).

Bending loads to surface. Optimization was performed for two different bending load cases, which were the bending loads $\mathbf{t} = -F\frac{\mathbf{x}}{|\mathbf{x}|}$ separately applied to each half of the concave surface of the hourglass-shaped domain (Fig 4).

Bending loads to edge. Optimization was performed for two different bending load cases, which were the bending loads $\mathbf{t} = -F\frac{\mathbf{x}}{|\mathbf{x}|}$ separately applied to each half of the edge of the hourglass-shaped domain (Fig 4).

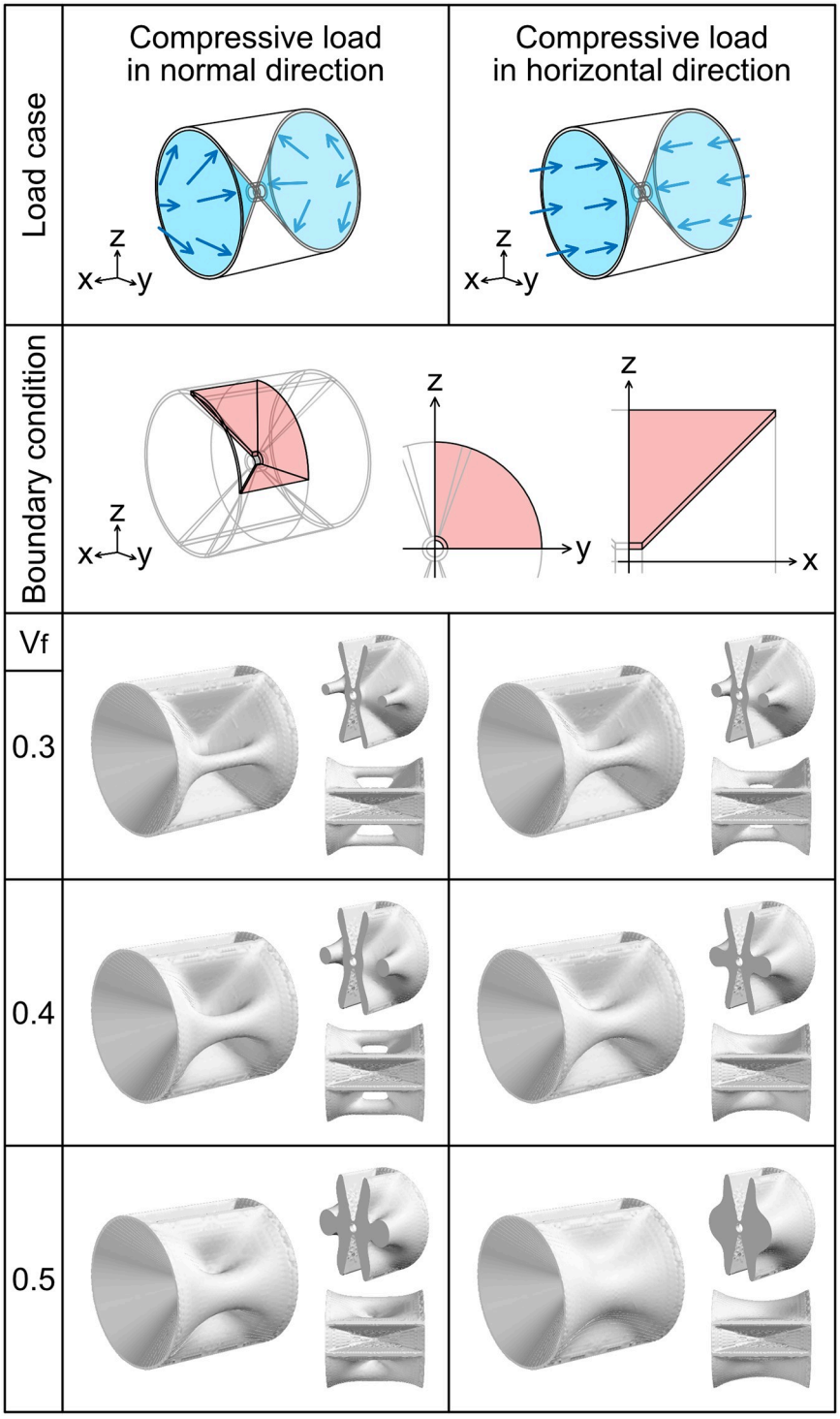

Fig 3. Optimization for compressive loads to autocentrum. The uppermost images are diagrams of the loads. The arrows indicate the load directions. The blue-colored area indicates where the load was applied. The images in the second row from the top show diagrams of the boundary condition; the boundary condition is the same in the two different compressive load cases. We imposed the symmetric boundary condition $\mathbf{u} \cdot \mathbf{n} = 0$ to the pink-colored area on the xy, yz, and zx planes and used an eighth model (left). The middle and right images in this row indicate the areas to which the symmetric boundary condition was imposed on the yz and zx plane, respectively. The area of the symmetric boundary condition on the xy plane is similar to that on the zx plane. The images in the third, fourth, fifth rows are the entire structures, transverse sections, and top views of the optimization results. The numbers in the leftmost column show the volume fraction.

https://doi.org/10.1371/journal.pcbi.1009043.g003

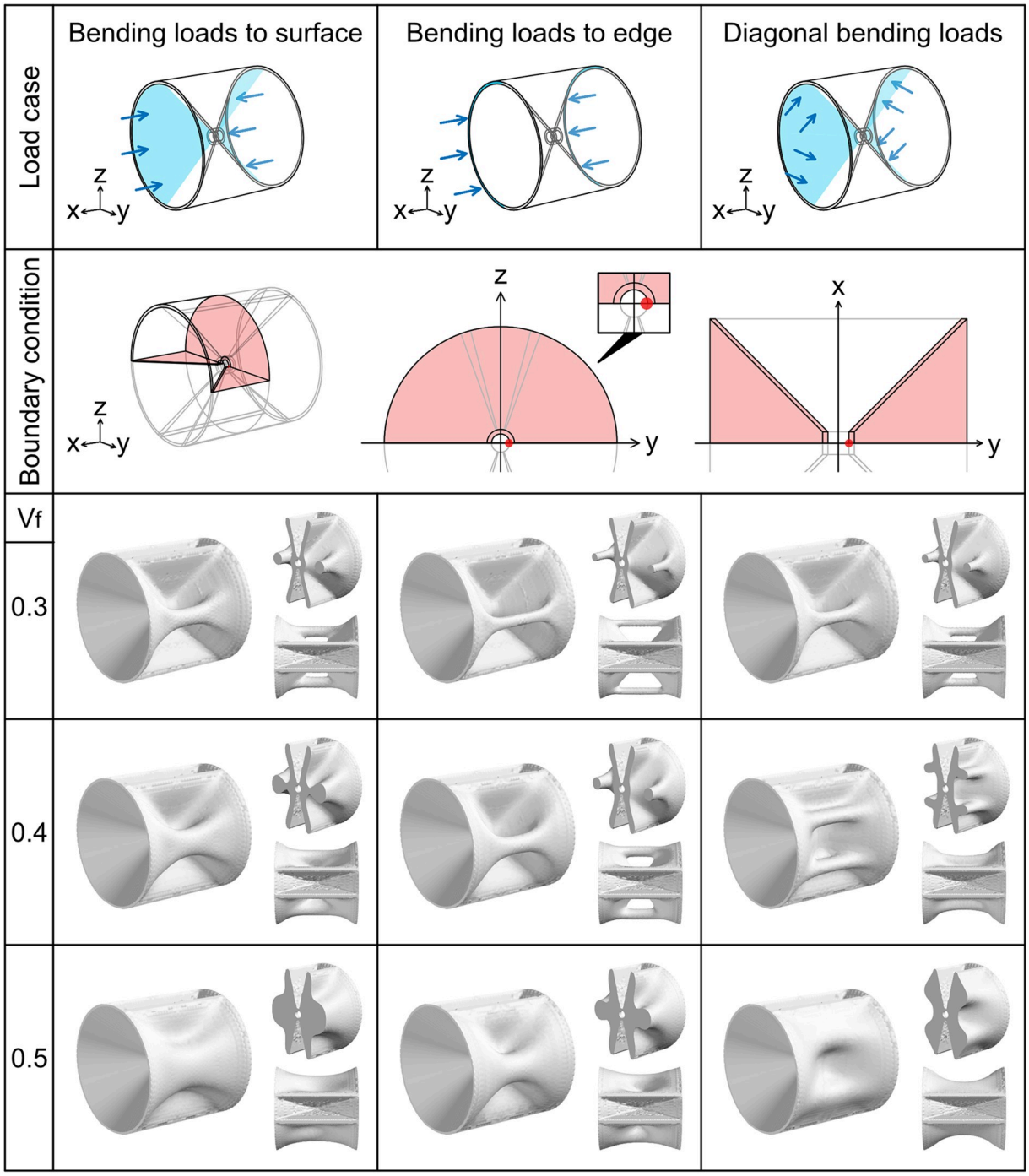

Fig 4. Optimization for bending loads to autocentrum. The arrangement and color scheme of the images are the same as those described in Fig 3. The boundary condition is the same in the three different bending load cases. We imposed the symmetric boundary condition $\mathbf{u} \cdot \mathbf{n} = 0$ on the xy and yz planes (left image in the second row from the top) and used a quarter model. The middle and right images in the second row from the top are the areas to which the symmetric boundary condition was imposed on the yz and xy plane, respectively. The magnified image of the center on the yz plane is shown. We imposed the displacement constraint $u_y = 0$ to the point $(0, C_R, 0)$ (red dot) when the bending loads $\mathbf{t} = -F\frac{\mathbf{x}}{|\mathbf{x}|}$ were applied to half of the concave surface of the hourglass-shaped domain in $y \leq 0$ (the blue-colored area). When we applied the bending loads to half of the area in $y \geq 0$, we imposed the same displacement constraint to the point $(0, -C_R, 0)$. In optimization for the diagonal bending loads, the results are displayed for $w = 0.8$.

https://doi.org/10.1371/journal.pcbi.1009043.g004

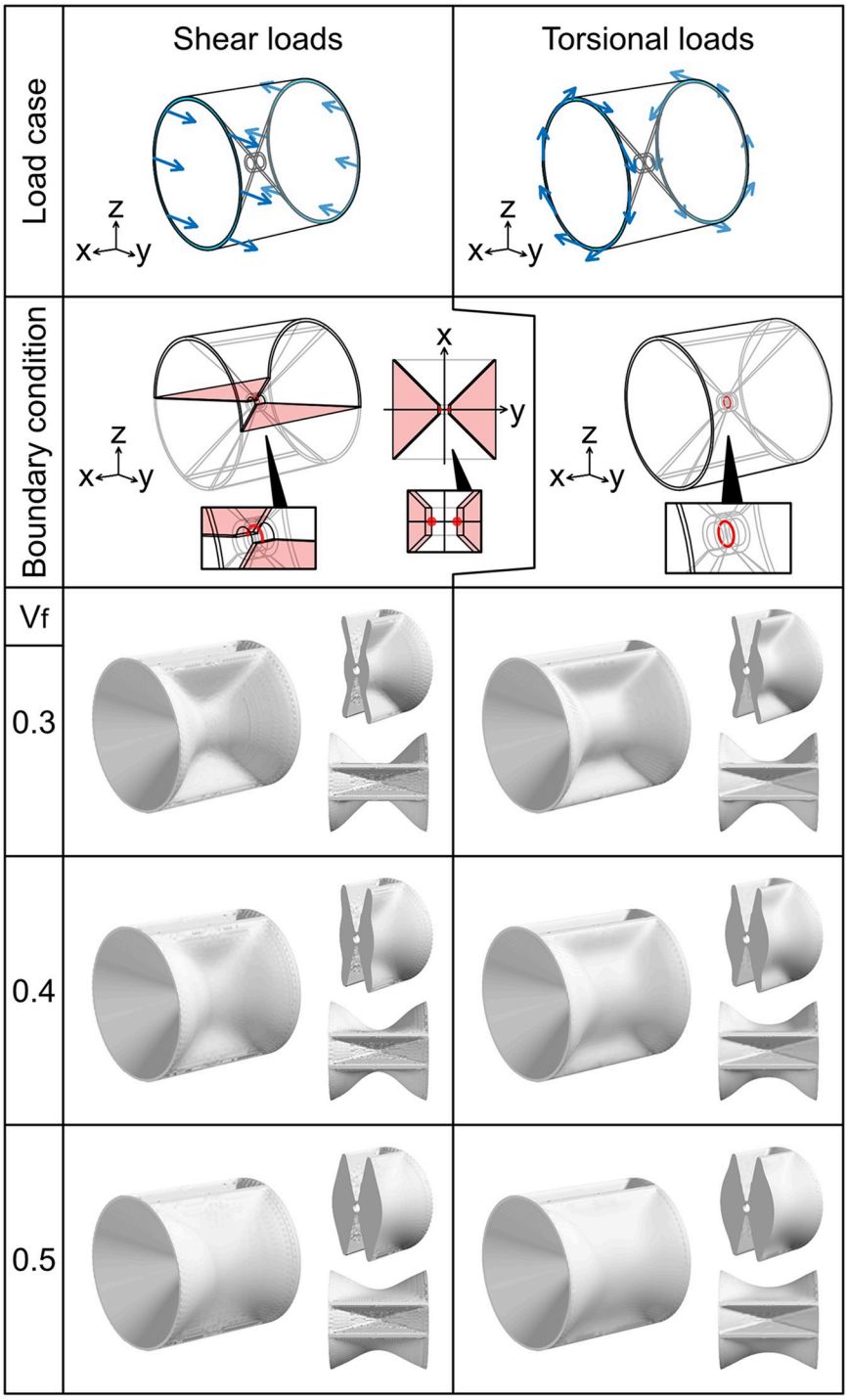

Fig 5. Optimization for shear and torsional loads to autocentrum. The arrangement and color scheme of the images are the same as those described in Fig 3. For the shear loads, we imposed the symmetric boundary condition $\mathbf{u} \cdot \mathbf{n} = 0$ on the xy plane (left image in the second row from the top) and used a half model. The right diagram is the area to which the symmetric boundary condition is imposed on the xy plane. Magnified images of the center of the analysis domain are shown. We imposed two displacement constraints: $u_x = 0$ to the points $(0, -C_R, 0)$ and $(0, C_R, 0)$ (the red dots), and $u_y = 0$ to the edge $y^2 + z^2 = C_R{}^2$ $(z \geq 0$, the red line). For the torsional loads, we imposed the displacement constraints $\mathbf{u} = 0$ to the edge $y^2 + z^2 = C_R{}^2$ (the red line).

https://doi.org/10.1371/journal.pcbi.1009043.g005

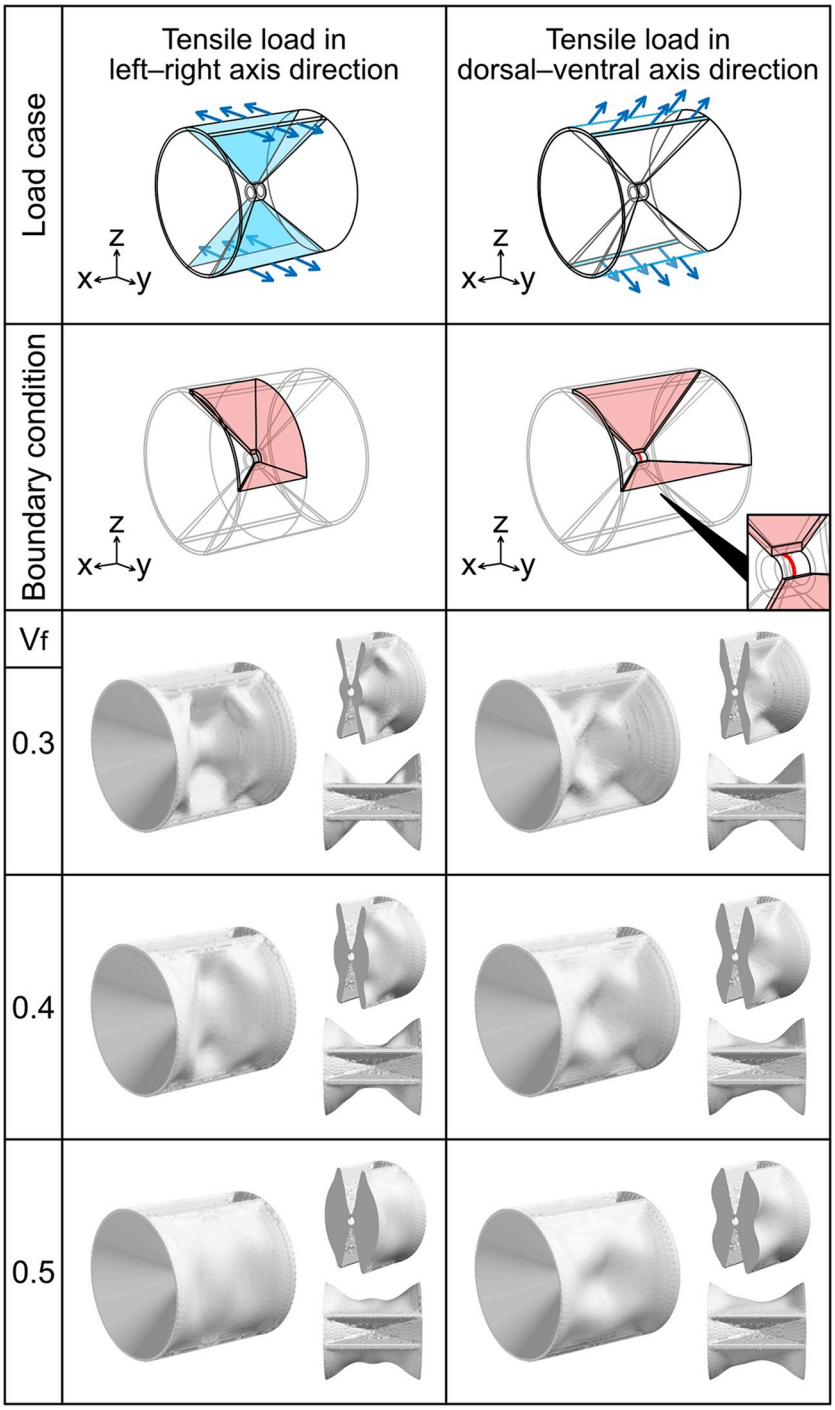

Fig 6. Optimization for tensile loads to vertebral arches. The arrangement and color scheme of the images are the same as those described in Fig 3. For the tensile load in left–right axis direction, we imposed the symmetric boundary condition $\mathbf{u} \cdot \mathbf{n} = 0$ to the pink-colored areas on the xy, yz, and zx planes and used an eighth model. For the tensile load in dorsal–ventral axis direction, we imposed the symmetric boundary condition to the pink-colored areas on the xy and zx planes and used a quarter model. We also imposed the displacement constraint $u_x = 0$ to the edge $y^2 + z^2 = C_R{}^2$ ($y \geq 0$ and $z \geq 0$, the red line). The bottom right of the second row shows the magnified image of the center of the analysis domain.

https://doi.org/10.1371/journal.pcbi.1009043.g006

Diagonal bending loads. Optimization was performed for two different load cases, which were the bending loads $\mathbf{t} = F\left(-\frac{\mathbf{x}}{|\mathbf{x}|} + w\frac{\mathbf{z}}{|\mathbf{z}|}\right)$ separately applied to each half of the concave surface of the hourglass-shaped domain (Fig 4). Here, $w \geq 0$ was the ratio of the vertical bending load to the horizontal bending load.

Shear loads. Optimization was performed for two different load cases: $\mathbf{t} = (0, F, 0)$ was applied to the edge in $x > 0$ and $\mathbf{t} = (0, -F, 0)$ was applied to the edge in $x < 0$ (Fig 5). Another load case was the counter direction of the former load case applied to the abovementioned regions.

Torsional loads. Optimization was performed for the clockwise and counterclockwise torsion. For the clockwise torsion, $\mathbf{t} = (0, \frac{F}{R}z, -\frac{F}{R}y)\ (x > 0)$ and $\mathbf{t} = \frac{F}{R}(0, -z, y)\ (x < 0)$ were applied to the edge of the autocentrum (Fig 5). R was the radius of the conical part: $R = C_T + C_R + Lsin(\theta)$. For the counterclockwise torsion, the counter direction of the former load case was applied to the abovementioned regions.

Tensile load to vertebral arches in left–right axis direction. A tensile load $\mathbf{t} = F\frac{\mathbf{y}}{|\mathbf{y}|}$ was applied to the external surface of the vertebral arches (Fig 6).

Tensile load to vertebral arches in dorsal–ventral axis direction. A tensile load $\mathbf{t} = (-F, 0, F\frac{z}{|z|})$ was applied to the distal edge of the vertebral arches (Fig 6).

Results

Optimization for different load cases

We initially attempted optimization for the load cases applied to the vertebral body (Figs 3–5). The optimization result for the compressive load in the normal direction exhibited a pillar structure on the lateral side of the vertebral body. The pillar structure became thicker as V_f increased. Moreover, the optimization result for the compressive load in the horizontal direction exhibited a pillar structure when $V_f = 0.3$, but the position of the pillar was close to the center of the vertebral body. When $V_f = 0.4$, the optimization result exhibited a plate-like ridge extending linearly from the center to the distal edge. When $V_f = 0.5$, the ridge was thicker and smoother.

The optimization result for the bending loads to the concave surface exhibited a pillar structure when $V_f = 0.3$. When $V_f = 0.4$, the optimization result had a plate-like ridge, which was thicker in the distal part than in the proximal part of the vertebral body. This structural feature resembled the lateral structure of the vertebral body of *Pagrus major* (Fig 1B, 1B' and 1B"). When $V_f = 0.5$, the ridge was thicker. The optimization result for the bending loads to the edge of the autocentrum exhibited a pillar structure on the lateral side far from the vertebral body center when $V_f = 0.3$ and $V_f = 0.4$. When $V_f = 0.5$, the optimization result exhibited a thick plate-like ridge extending from the vertebral body center to the distal edge. Furthermore, we attempted optimization for the diagonal bending loads with a vertically bending load in addition to the horizontally bending load (Fig 4). We adjusted the ratio of the vertically bending load to the horizontally bending load w. When the ratio was small (w was 0.1 to 0.6), the optimized structure exhibited a pillar structure. However, when the ratio was $w = 0.7$ and $V_f = 0.4$, two pillar structures were formed. When the ratio w was 0.8 to 1.0 and $V_f = 0.4$, two plate-like ridges were formed (Fig 4). These two plate-like ridges were similar to the lateral structure of the vertebral body of *Zenopsis nebulosa* (Fig 1D, 1D' and 1D"). When $V_f = 0.5$, two thick ridges were formed.

In addition to the reproduction of plate-like ridges, we observed structural variation depending on the amount of available material. The optimization for the horizontal compressive loads or bending loads produced plate-like ridges when $V_f = 0.4$ and $V_f = 0.5$. However,

when $V_f = 0.3$, the optimization results exhibited a pillar structure in which the material at the proximal part was removed. In certain teleost species, the lateral structure of the vertebral bodies has internal hollow spaces, in which bone has been removed [49]. Our topology optimization model produced a similar structural feature to the internal hollow spaces.

In the optimization result for the shear loads, the material was added almost uniformly to the hourglass-shaped domain and no pillar or ridge was formed (Fig 5). The optimization result for the torsional loads was similar, but the proximal part of the vertebral body was thicker than that in the optimization result for the shear loads (Fig 5).

We further investigated the optimization for load cases applied to the vertebral arches (Fig 6). The optimization result for the tensile load in the left–right axis direction indicated that four small hump-like ridges were formed on the edges of the vertebral body. When $V_f = 0.4$, thicker hump-like ridges were formed (Fig 6). This structural feature was observed in the vertebral body of *Scarus forsteni* (Fig 1F and 1F'). When $V_f = 0.5$, the material was added uniformly to the hourglass-shaped domain. Moreover, the optimization result for the tensile load in the dorsal–ventral axis direction along the vertebral arches exhibited four diagonal ridges extending from the vertebral arches to the vertebral body when $V_f = 0.3$. These four ridges crossed one another (Fig 6). This structural feature was similar to the tarp-like triangle ridges of the vertebral body of *Macroramphosus sagifue* (Fig 1G and 1G'). When $V_f = 0.4$ and $V_f = 0.5$, the four ridges were thick.

Optimization in different analysis domains

To apply our model to the simulation of the external shapes of bones, model validation is an important step. Although we reproduced the morphological features of the teleost vertebrae by setting different load cases, it is difficult to measure the external load condition of real fish. Therefore, we focused on the geometric parameters of the analysis domain. A previous comparative observation of teleost vertebrae [49] showed that geometric parameters such as the aspect ratio of the vertebral bodies and the gap width of the vertebral arches differ among species. In the simulations described above, the vertebral arches and autocentrum were predefined. However, when these geometric parameters change, the calculation results also change. Hence, we can validate our model by comparing the simulation results for different geometric parameters with real teleost vertebrae.

In many teleost species, the gap width of the vertebral arches is in the range of 30˚ to 60˚ (S2 Fig). Accordingly, we adjusted the half gap width parameter η to range from 15˚ to 32.5˚ (the gap width was 2η). Optimization for the bending loads to the autocentrum surface exhibited a pillar structure when the gap width was relatively small (Fig 7A; see also Fig 4). However, when the gap width was larger at 60˚, a thin plate-like ridge was produced. This thin plate-like ridge was observed in the vertebral body of *Acropoma hanedai* (Fig 1C and 1C'). In fact, the gap width of *Acropoma hanedai* is larger than that of *Pagrus Major* (See S1 Data). Note that we compared the gap width of the dorsal arch because the gap width of the ventral arches greatly varies according to the anatomical position. Moreover, we attempted optimization for the tensile load to the vertebral arches in the left–right axis direction. When the gap width was small, the optimization result exhibited hump-like structures on the edges of the vertebral body (Fig 7B). However, when the gap width was 50˚, a transverse pillar structure was produced. Moreover, when the gap width was larger than 55˚, a transverse plate-like ridge extending from the vertebral body center was produced. A transverse plate-like ridge was observed in the vertebral body of *Muraenesox cinereus* (Fig 1E and 1E'). In fact, the gap width of *Muraenesox cinereus* is larger than that of *Scarus forsteni*. Therefore, the dependence on this parameter matches the relationship between the gap width and the lateral structure of teleost vertebrae.

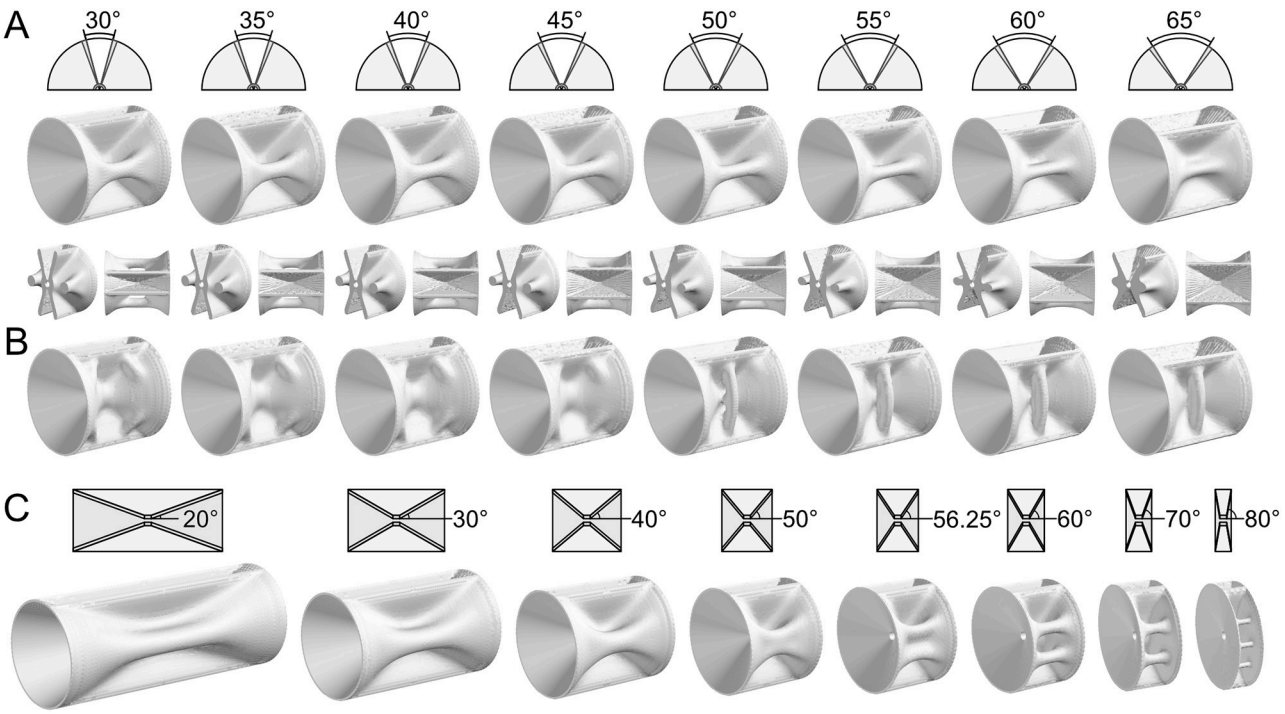

Fig 7. Dependence of lateral structure of vertebral bodies on analysis domain geometry. (A and B) Adjusting the gap width of vertebral arches η. The load case was (A) the bending loads to the autocentrum surface in the horizontal direction and (B) the tensile load to the vertebral arches in the left–right axis direction. The optimization results are displayed every five degrees. In (A), the transverse sections and top views are also displayed. (C) Adjusting the vertebral body lengths in the cranial–caudal direction. The value of θ is displayed. The volume fraction V_f is 0.33 in (A), 0.3 in (B), and 0.4 in (C).

https://doi.org/10.1371/journal.pcbi.1009043.g007

The autocentrum length in the cranial–caudal direction varies among teleost species [46, 49] (S1 Fig). Because our model could imitate this variation by adjusting the cone angle θ, we adjusted θ by setting identical vertebral lengths in the dorsal–ventral direction $L(\theta) = \mathrm{L}\frac{\sin\frac{\pi}{4}}{\sin\theta}$ (Fig 7C). The optimization results for the bending loads to the autocentrum surface exhibited a thick plate-like ridge on the lateral side when the vertebral length was large (θ was 20 to 40˚). When the vertebral length was small, the lateral structure varied from the pillar structure to the divided two-pillar structures (θ was 50 to 70˚), and when the vertebral length was very small, the divided three-pillar structures were produced (θ was 80˚). Indeed, the long vertebral bodies of some Perciformes species have no or only one lateral ridge, whereas the short vertebral bodies of some Zeiformes and Pleuronectiformes species have multiple lateral ridges (See Figure 2 of [49]). Based on these simulation results, we verified that our model can demonstrate the variation in the lateral structures of teleost vertebrae.

Discussion

In this study, we constructed a 3D topology optimization model for the reproduction of teleost vertebrae to test whether the 3D external bone shape can be reproduced using a mathematical model imitating bone formation that depends on external loads. Our topology optimization model produced a variety of 3D structures based on stiffness maximizations for different load cases, and some of these structures exhibited structural features that were similar to the lateral structures of teleost vertebral bodies. This result shows that topology optimization can be applied to reproduce 3D bone external shapes, which can be used to demonstrate the

adaptation of bone external shape to external loads. In addition, the variation in lateral structures was reproduced by the difference in load cases and in the shape of the bone parts that are formed independently of external loads. This suggests that our model can be used to explain how adaptation to the external loads and development based on gene expression influence the variation in the shapes of teleost vertebrae.

Bone internal structure and external shape

Because the internal trabecular bone and the external cortical bone exhibit different structural features, several studies have compared the formation process between these bones [66–68]. However, these bones are similarly formed by osteoblasts and osteoclasts. Furthermore, several studies have reported that the trabecular bones coalesce into the cortical bone in the young growing long bones and jawbones of mammals [69–71]. Based on these facts, some researchers hypothesized that a similar mechanism forms the trabecular and cortical bones. Tanck et al. [72] reproduced the continuous structural changes from the trabecular bones to cortical bones using the bone remodeling algorithm, showing that the thin pillar structures change into thick structures with increasing external loads.

In this study, we reproduced the pillar structure similar to the trabecular bones and the thick plate-like ridges separately, suggesting that the trabecular and cortical bones are indeed formed by a similar mechanism. However, it is difficult to produce a structure with both the thin pillar and thick structural features. In our topology optimization model, the minimum thickness of the structures is regulated by the diffusion term for smoothing the material distribution [55]. We can then adjust the diffusion coefficient to investigate how the extent of bone synthesis and resorption influences bone shape, which relates to the group size of osteoblasts and osteoclasts. To decrease the diffusion coefficient, we need to use the fine mesh that discretizes the design domain. However, simulation with many fine meshes is time-consuming, taking days; thus, fine mesh is not suitable for testing optimizations for different load cases. Therefore, we used the relatively coarse mesh in this study. However, our model could reproduce both the trabecular and cortical bones simultaneously by decreasing the diffusion coefficient and using fine meshes. We previously reported that some species such as tuna have vertebrae in which the internal trabecular bones are covered by the external cortical bones [49]. By reproducing this structure, we can explain the formation of the trabecular and cortical bones according to the variation in the behaviors of osteoblasts and osteoclasts.

Future improvements to our model

In this study, we used a very simple algorithm in which fewer principles were considered compared with other mathematical models [23, 37, 73] to investigate the dependence of the variation in bone external shapes on load condition. For this reason, our model reproduced only a limited number of the lateral structures of teleost vertebrae. Recent studies have considered more factors for more accurate simulations, such as the intercellular signaling [74], the osteocytic mechanosensory system [75, 76], the site-specific effect on bone formation [77], and the material properties of bones [78–80]. Following these perspectives, our model may be able to reproduce more types of lateral structures by considering additional factors relating to teleost vertebrae.

For instance, we previously found that the lateral structures of most teleost species have equally spaced microcracks extending in the radial direction from the center of the vertebral bodies [49]. This finding suggests that the growth direction of teleost vertebral bodies has a radial anisotropy, which does not depend on external loads. In anglerfish and pufferfish, the lateral structure exhibits a net-like shape that is formed by many thin sheet-like trabeculae

extending radially from the center of the vertebral body [49]. Because these species hardly undulate their bodies during swimming [81], we assume that factors other than adaptation to muscle tension influence the formation of the net-like lateral structure. Therefore, introducing anisotropic growth of the vertebrae into our model may allow for reproduction of the net-like structure.

In addition to modifications of the model, we can attempt optimization for different complex load cases and different objectives [82]. For these reasons, topology optimization can be applied to the computer simulations of bone shapes in a variety of vertebrate species. Further studies using computer simulations will help to understand the relationship between bone shapes and external loads.

Estimating the external loads

Elucidating bone external loads is necessary to understand how bones support the body of vertebrates. Because it is difficult to examine external loads directly, researchers have speculated the external loads based on anatomical observations. For instance, Laerm [46] described that the lateral structure of teleost vertebral bodies adapts to the bending load exerted by fish undulations. This speculation was based on morphological observations of the vertebrae, and it has not been examined. However, our simulation results demonstrated that the bending load is important for formation of the plate-like ridge, thereby supporting Laerm's speculation. By comparing the optimization results and the teleost vertebrae, we can examine the external loads that are significant to the formation of the teleost vertebrae.

Moreover, other studies have developed methods to calculate the external loads from motion capture [83–86] and from an *ex vivo* loading test [87–89]. We can also utilize these methods to confirm whether our simulation accurately estimates external loads.

Accurate estimation of the external loads will help to improve conventional structural analysis of teleost vertebrae [10, 64], in which the external load condition was speculated based on anatomical observations. Such improved analyses will help to explain the mechanism that maintains the body balance of vertebrates. Implementing the simulations and analyses of the vertebrae in a broader range of teleost species may further help to estimate the locomotion styles of fish.

Relationship between vertebrae shapes and swimming styles

In teleosts, swimming style greatly varies among species [81]. Previous anatomical studies have shown that according to the swimming styles, species exhibit different material property, morphology, arrangement, and deformation pattern of the lateral muscle and connective tissues [90–95]. These differences in the surrounding tissues can impose different external loads on the vertebrae. In our simulation, the optimizations for the different load cases reproduced the different lateral structures of the vertebral bodies. These findings can lead to a hypothesis that teleost vertebrae adapt these shapes to the external loads determined by swimming styles. If so, we can explain the swimming styles of the extinct species based on the shapes of the vertebrae. Furthermore, we may understand how teleosts have obtained different swimming styles in the phylogenetic history. To confirm this hypothesis, further investigation of whether changes in swimming style can induce changes in vertebrae shape should be performed.

Materials and methods

Skeletal specimens of fish

All fish were obtained via commercial bottom trawling in the coast of the Japan archipelago, or purchased from fish markets in Japan. Fish identification followed [96]. To prepare the skeletal specimens, we first boiled the fish for approximately 15 to 30 min, depending on the size of fish, until the body tissues were completely heated. Then, we roughly removed the muscles, and the bones were cleaned by immersion in trypsin solution (trypsin [BECTON DICKINSON Difco Trypsin 250] 1 g in milliQ) for 1 day. We then removed the remaining tissues using running water and air-dried the bones at room temperature (24–25˚C).

Micro-CT scanning

We scanned the skeletal specimens of vertebral bodies from each individual fish using the micro-CT scanner SkyScan 1,172 (SkyScan NV, Aartselaar, Belgium) following the manufacturer's instructions. For stable positioning, we fixed each specimen to the stage using double-sided tape. The X-ray source was 50 kV, and the datasets were acquired at a resolution of 2.48 to 10.9 μm/pixel, depending on the size of each vertebral body. We reconstructed the transverse section stacks from primary shadow images using the SkyScan software NRecon (Version 1.7.1.0). From these image stacks, we constructed 3D volume-rendered images using the SkyScan software CTVox (Version 3.3.0).

Supporting information

S1 Text. Topology optimization method with time-dependent diffusion equation.
(PDF)

S1 Code. Code for the simulation. By running this MATLAB script file in LiveLink for MATLAB, we can implement the optimization for compressive load in normal direction. Also, it generates a COMSOL Multiphysics binary file. By editing this binary file, we performed all simulations in this paper. We used COMSOL Multiphysics version 5.4 and MATLAB R2018b.
(M)

S1 Fig. Analysis of angle of the conical parts of vertebral body. (A) Method for measuring angle of conical parts. We defined three points to draw lines along the cone and measured the angle (white lines) using the angle tool of ImageJ (https://imagej.nih.gov/ij/). We measured the angles of cranial conical part and caudal conical part. The positions of the vertices at these angles are different in some species because the central part of the vertebral bodies is not exactly straight. (B) Ratio of angle of conical part. We used the vertebral body with the first hemal arch of 32 teleost species. Original measurement data are presented in S1 Data.
(TIFF)

S2 Fig. Analysis of gap width of vertebral arches. (A) Method for measuring gap width of vertebral arches. We defined three points to draw lines along the vertebral arch and measured the angle (white lines) using the angle tool of ImageJ (https://imagej.nih.gov/ij/). We measured the angles of dorsal arch and hemal arch. The positions of the vertices at these angles are different in some species because the positions of vertebral arches are not exactly symmetrical. (B) Ratio of gap width of vertebral arches. We used the vertebral body with the first hemal arch of 32 teleost species. Original measurement data are presented in S1 Data.
(TIFF)

S3 Fig. Effect of initial density values on optimization results. To investigate the effect of the different initial density values, we adjusted the initial density value in the range of $d \leq \rho \leq 1$. The optimization for the diagonal bending loads produced different structures to those shown in Fig 4 when the initial density value in the design domain was $\rho = 1$. When $V_f = 0.4$, the result exhibited a pillar structure. In other initial density values, the optimization results were the same as those shown in Fig 4. These different structures are local optima for stiffness maximization, among which the convergent values of the compliance are similar. In this load case, the initial density value influences shape variation. However, the other optimizations performed in this study were not influenced by the initial density values, producing the same structure as those shown in Figs 3–7.
(TIFF)

S1 Data. Angle of the conical parts of the vertebral body and gap width of the vertebral arches in 32 teleost species. To obtain these data, we used the micro-CT sections of the vertebrae with the first hemal arch of 32 teleost species. The sections are provided in the SSBD database (http://ssbd.qbic.riken.jp/set/20190301/) (See [49]).
(XLSX)

S1 Video. Optimization process for compressive load in normal direction.
(GIF)

Acknowledgments

We thank Dr. Tsuguo Kondoh, Dr. Tsuyoshi Nomura, Shun Maruyama, and Hiroki Kobayashi for their helpful advice and the continuous discussion of mathematical modeling using topology optimization. We also thank Dr. Mao Sato for providing the fish.

Author Contributions

Conceptualization: Misaki Sakashita, Shigeru Kondo.

Data curation: Misaki Sakashita.

Formal analysis: Misaki Sakashita.

Funding acquisition: Shigeru Kondo.

Investigation: Misaki Sakashita.

Methodology: Shintaro Yamasaki, Kentaro Yaji, Atsushi Kawamoto.

Project administration: Misaki Sakashita, Shigeru Kondo.

Resources: Shigeru Kondo.

Software: Misaki Sakashita.

Supervision: Shigeru Kondo.

Validation: Misaki Sakashita.

Visualization: Misaki Sakashita.

Writing – original draft: Misaki Sakashita.

Writing – review & editing: Misaki Sakashita, Shintaro Yamasaki, Kentaro Yaji, Atsushi Kawamoto, Shigeru Kondo.

References

1. Shiba D, Mizuno H, Yumoto A, Shimomura M, Kobayashi H, Morita H, et al. Development of new experimental platform 'MARS'—Multiple Artificial-gravity Research System—to elucidate the impacts of micro/partial gravity on mice. Scientific Reports. 2017; 7(1):10837. https://doi.org/10.1038/s41598-017-10998-4 PMID: 28883615
2. Gerbaix M, Gnyubkin V, Farlay D, Olivier C, Ammann P, Courbon G, et al. One-month spaceflight compromises the bone microstructure, tissue-level mechanical properties, osteocyte survival and lacunae volume in mature mice skeletons. Scientific Reports. 2017; 7(1):2659. https://doi.org/10.1038/s41598-017-03014-2 PMID: 28572612
3. Biggin A, Briody JN, Ramjan KA, Middleton A, Waugh MCA, Munns CF. Evaluation of bone mineral density and morphology using pQCT in children after spinal cord injury. Developmental Neurorehabilitation. 2013; 16(6):391–397. https://doi.org/10.3109/17518423.2012.762590
4. Slijper EJ. Biologic-anatomical investigations on the bipedal gait and upright posture in mammals, with special reference to a little goat, born without forelegs II. Proceedings of the Koninklijke Nederlandse Akademie Van Wetenschappen. 1942; 45:407–415.
5. Skerry TM, Lanyon LE, Bitensky L, Chayen J. Early strain-related changes in enzyme activity in osteocytes following bone loading in vivo. Journal of Bone and Mineral Research. 1989; 4(5):783–788. https://doi.org/10.1002/jbmr.5650040519
6. Bonewald LF. The amazing osteocyte. Journal of Bone and Mineral Research. 2011; 26(2):229–238. https://doi.org/10.1002/jbmr.320
7. Shahar R, Dean MN. The enigmas of bone without osteocytes. BoneKEy reports. 2013; 2:343. https://doi.org/10.1038/bonekey.2013.168
8. Plotkin LI, Bellido T. Osteocytic signalling pathways as therapeutic targets for bone fragility. Nature Reviews Endocrinology. 2016; 12(10):593–605. https://doi.org/10.1038/nrendo.2016.71
9. Atkins A, Milgram J, Weiner S, Shahar R. The response of anosteocytic bone to controlled loading. Journal of Experimental Biology. 2015; 218(22):3559–3569. https://doi.org/10.1242/jeb.124073
10. Ofer L, Dean MN, Zaslansky P, Kult S, Shwartz Y, Zaretsky J, et al. A novel nonosteocytic regulatory mechanism of bone modeling. PLOS Biology. 2019; 17(2):1–22. https://doi.org/10.1371/journal.pbio.3000140 PMID: 30707688
11. Robling AG, Niziolek PJ, Baldridge LA, Condon KW, Allen MR, Alam I, et al. Mechanical Stimulation of Bone in Vivo Reduces Osteocyte Expression of Sost/Sclerostin. Journal of Biological Chemistry. 2008; 283(9):5866–5875. https://doi.org/10.1074/jbc.M705092200 PMID: 18089564
12. Aguirre JI, Plotkin LI, Stewart SA, Weinstein RS, Parfitt AM, Manolagas SC, et al. Osteocyte Apoptosis Is Induced by Weightlessness in Mice and Precedes Osteoclast Recruitment and Bone Loss. Journal of Bone and Mineral Research. 2006; 21(4):605–615. https://doi.org/10.1359/jbmr.060107 PMID: 16598381
13. Tatsumi S, Ishii K, Amizuka N, Li M, Kobayashi T, Kohno K, et al. Targeted Ablation of Osteocytes Induces Osteoporosis with Defective Mechanotransduction. Cell Metabolism. 2007; 5(6):464–475. https://doi.org/10.1016/j.cmet.2007.05.001 PMID: 17550781
14. Roux W. Der Kampf der Theile im Organismus. Engelmann Leipzig; 1881.
15. Roesler H. The history of some fundamental concepts in bone biomechanics. Journal of Biomechanics. 1987; 20(11):1025–1034. https://doi.org/10.1016/0021-9290(87)90020-0
16. Lee TC, Taylor D. Bone remodelling: Should we cry wolff? Irish Journal of Medical Science. 1999; 168(2):102. https://doi.org/10.1007/BF02946474
17. Huiskes R. If bone is the answer, then what is the question? Journal of Anatomy. 2000; 197(2):145–156. https://doi.org/10.1046/j.1469-7580.2000.19720145.x
18. Meyer GH. Die Architektur der spongiosa. Arch Anat Physiol Wiss Med. 1867; 34:615–628.
19. Wolff J. The Law of Bone Remodelling. Springer-Verlag Berlin Heidelberg; 1986.
20. Huiskes R, Weinans H, Grootenboer HJ, Dalstra M, Fudala B, Slooff TJ. Adaptive bone-remodeling theory applied to prosthetic-design analysis. Journal of Biomechanics. 1987; 20(11):1135–1150. https://doi.org/10.1016/0021-9290(87)90030-3
21. Weinans H, Huiskes R, Grootenboer HJ. The behavior of adaptive bone-remodeling simulation models. Journal of Biomechanics. 1992; 25(12):1425–1441. https://doi.org/10.1016/0021-9290(92)90056-7
22. Mullender MG, Huiskes R, Weinans H. A physiological approach to the simulation of bone remodeling as a self-organizational control process. Journal of Biomechanics. 1994; 27(11):1389–1394. https://doi.org/10.1016/0021-9290(94)90049-3

23. Huiskes R, Ruimerman R, van Lenthe GH, Janssen JD. Effects of mechanical forces on maintenance and adaptation of form in trabecular bone. Nature. 2000; 405(6787):704–706. https://doi.org/10.1038/35015116

24. Ruimerman R, Hilbers P, van Rietbergen B, Huiskes R. A theoretical framework for strain-related trabecular bone maintenance and adaptation. Journal of Biomechanics. 2005; 38(4):931–941. https://doi.org/10.1016/j.jbiomech.2004.03.037

25. Mattheck C, Reuss S. The claw of the tiger: An assessment of its mechanical shape optimization. Journal of Theoretical Biology. 1991; 150(3):323–328. https://doi.org/10.1016/S0022-5193(05)80431-X

26. Mattheck C. Design in Nature. Springer-Verlag Berlin Heidelberg; 1998. https://doi.org/10.1007/978-3-642-58747-4

27. Hollister SJ, Kikuchi N, Goldstein SA. Do bone ingrowth processes produce a globally optimized structure? Journal of Biomechanics. 1993; 26(4):391–407. https://doi.org/10.1016/0021-9290(93)90003-W

28. Hollister SJ, Kikuchi N. Homogenization theory and digital imaging: A basis for studying the mechanics and design principles of bone tissue. Biotechnology and Bioengineering. 1994; 43(7):586–596. https://doi.org/10.1002/bit.260430708

29. Hollister SJ, Brennan JM, Kikuchi N. A homogenization sampling procedure for calculating trabecular bone effective stiffness and tissue level stress. Journal of Biomechanics. 1994; 27(4):433–444. https://doi.org/10.1016/0021-9290(94)90019-1

30. Bagge M. A model of bone adaptation as an optimization process. Journal of Biomechanics. 2000; 33 (11):1349–1357. https://doi.org/10.1016/S0021-9290(00)00124-X

31. Jang IG, Kim IY. Computational study of Wolff's law with trabecular architecture in the human proximal femur using topology optimization. Journal of Biomechanics. 2008; 41(11):2353–2361. https://doi.org/10.1016/j.jbiomech.2008.05.037

32. Jang IG, Kim IY. Computational simulation of simultaneous cortical and trabecular bone change in human proximal femur during bone remodeling. Journal of Biomechanics. 2010; 43(2):294–301. https://doi.org/10.1016/j.jbiomech.2009.08.012

33. Boyle C, Kim IY. Three-dimensional micro-level computational study of Wolff's law via trabecular bone remodeling in the human proximal femur using design space topology optimization. Journal of Biomechanics. 2011; 44(5):935–942. https://doi.org/10.1016/j.jbiomech.2010.11.029

34. Bendsøe MP, Kikuchi N. Generating optimal topologies in structural design using a homogenization method. Computer Methods in Applied Mechanics and Engineering. 1988; 71(2):197–224. https://doi.org/10.1016/0045-7825(88)90086-2

35. Bendsøe MP. Optimal shape design as a material distribution problem. Structural optimization. 1989; 1 (4):193–202. https://doi.org/10.1007/BF01650949

36. Jang IG, Kim IY, Kwak BM. Analogy of Strain Energy Density Based Bone-Remodeling Algorithm and Structural Topology Optimization. Journal of Biomechanical Engineering. 2008; 131(1). https://doi.org/10.1115/1.3005202

37. Gerhard FA, Webster DJ, van Lenthe GH, Müller R. *In silico* biology of bone modelling and remodelling: adaptation. Philosophical Transactions of the Royal Society A: Mathematical, Physical and Engineering Sciences. 2009; 367(1895):2011–2030. https://doi.org/10.1098/rsta.2008.0297

38. Kameo Y, Tsubota K, Adachi T. Bone Adaptation: In Silico Approach. Springer Japan Tokyo; 2018. https://doi.org/10.1007/978-4-431-56514-7

39. Garcia JM, Martìnez MA, Doblarè M. An Anisotropic Internal-External Bone Adaptation Model Based on a Combination of CAO and Continuum Damage Mechanics Technologies. Computer Methods in Biomechanics and Biomedical Engineering. 2001; 4(4):355–377. https://doi.org/10.1080/10255840108908014

40. Xinghua Z, He G, Dong Z, Bingzhao G. A study of the effect of non-linearities in the equation of bone remodeling. Journal of Biomechanics. 2002; 35(7):951–960. https://doi.org/10.1016/S0021-9290(02)00028-3

41. Xinghua Z, He G, Bingzhao G. The application of topology optimization on the quantitative description of the external shape of bone structure. Journal of Biomechanics. 2005; 38(8):1612–1620. https://doi.org/10.1016/j.jbiomech.2004.06.029

42. Carpenter RD, Carter DR. Computational simulation of spontaneous bone straightening in growing children. Biomechanics and Modeling in Mechanobiology. 2010; 9(3):317–328. https://doi.org/10.1007/s10237-009-0178-x

43. Mittag U, Kriechbaumer A, Bartsch M, Rittweger J. Form follows function: a computational simulation exercise on bone shape forming and conservation. Journal of Musculoskeletal and Neuronal Interactions. 2015; 15:215–226.

44. Mittag U, Kriechbaumer A, Rittweger J. Torsion—an underestimated form shaping entity in bone adaptation? Journal of Musculoskeletal and Neuronal Interactions. 2018; 18:407–418.

45. Nordvik K, Kryvi H, Totland GK, Grotmol S. The salmon vertebral body develops through mineralization of two preformed tissues that are encompassed by two layers of bone. Journal of Anatomy. 2005; 206 (2):103–114. https://doi.org/10.1111/j.1469-7580.2005.00372.x

46. Laerm J. The development, function, and design of amphicoelous vertebrae in teleost fishes1. Zoological Journal of the Linnean Society. 1976; 58(3):237–254. https://doi.org/10.1111/j.1096-3642.1976.tb00830.x

47. Arratia G, Schultze HP, Casciotta J. Vertebral column and associated elements in dipnoans and comparison with other fishes: Development and homology. Journal of Morphology. 2001; 250(2):101–172. https://doi.org/10.1002/jmor.1062

48. Eastman JT, Witmer LM, Ridgely RC, Kuhn KL. Divergence in skeletal mass and bone morphology in antarctic notothenioid fishes. Journal of Morphology. 2014; 275(8):841–861. https://doi.org/10.1002/jmor.20258

49. Sakashita M, Sato M, Kondo S. Comparative morphological examination of vertebral bodies of teleost fish using high-resolution micro-CT scans. Journal of Morphology. 2019; 280(6):778–795. https://doi.org/10.1002/jmor.20983

50. Rockwell H, Evans FG, Pheasant HC. The comparative morphology of the vertebrate spinal column. Its form as related to function. Journal of Morphology. 1938; 63(1):87–117. https://doi.org/10.1002/jmor.1050630105

51. Shadwick RE, Lauder GV. Fish biomechanics. Amsterdam; Boston: Academic Press; 2006.

52. Fiedler IAK, Schmidt FN, Wölfel EM, Plumeyer C, Milovanovic P, Gioia R, et al. Severely Impaired Bone Material Quality in Chihuahua Zebrafish Resembles Classical Dominant Human Osteogenesis Imperfecta. Journal of Bone and Mineral Research. 2018; 33(8):1489–1499. https://doi.org/10.1002/jbmr.3445 PMID: 29665086

53. Cotti S, Huysseune A, Koppe W, Rücklin M, Marone F, Wölfel EM, et al. More Bone with Less Minerals? The Effects of Dietary Phosphorus on the Post-Cranial Skeleton in Zebrafish. International Journal of Molecular Sciences. 2020; 21(15). https://doi.org/10.3390/ijms21155429 PMID: 32751494

54. Bendsøe MP, Sigmund O. Material interpolation schemes in topology optimization. Archive of Applied Mechanics. 1999; 69(9):635–654. https://doi.org/10.1007/s004190050248

55. Kawamoto A, Matsumori T, Nomura T, Kondoh T, Yamasaki S, Nishiwaki S. Topology optimization by a time-dependent diffusion equation. International Journal for Numerical Methods in Engineering. 2013; 93(8):795–817. https://doi.org/10.1002/nme.4407

56. Fleming A, Kishida MG, Kimmel CB, Keynes RJ. Building the backbone: the development and evolution of vertebral patterning. Development. 2015; 142(10):1733–1744. https://doi.org/10.1242/dev.118950

57. Grotmol S, Kryvi H, Nordvik K, Totland GK. Notochord segmentation may lay down the pathway for the development of the vertebral bodies in the Atlantic salmon. Anatomy and Embryology. 2003; 207 (4):263–272. https://doi.org/10.1007/s00429-003-0349-y

58. Willems B, Büttner A, Huysseune A, Renn J, Witten PE, Winkler C. Conditional ablation of osteoblasts in medaka. Developmental Biology. 2012; 364(2):128–137. https://doi.org/10.1016/j.ydbio.2012.01.023

59. Chatani M, Mantoku A, Takeyama K, Abduweli D, Sugamori Y, Aoki K, et al. Microgravity promotes osteoclast activity in medaka fish reared at the international space station. Scientific Reports. 2015; 5 (1):14172. https://doi.org/10.1038/srep14172 PMID: 26387549

60. Turko AJ, Kültz D, Fudge D, Croll RP, Smith FM, Stoyek MR, et al. Skeletal stiffening in an amphibious fish out of water is a response to increased body weight. Journal of Experimental Biology. 2017; 220 (20):3621–3631. https://doi.org/10.1242/jeb.161638

61. Schmitz RJ. Ultrastructure and function of cellular components of the intercentral joint in the percoid vertebral column. Journal of Morphology. 1995; 226(1):1–24. https://doi.org/10.1002/jmor.1052260102

62. Schmitz RJ. Immunohistochemical identification of the cytoskeletal elements in the notochord cells of bony fishes. Journal of Morphology. 1998; 236(2):105–116. https://doi.org/10.1002/(SICI)1097-4687(199805)236:2%3C105::AID-JMOR2%3E3.0.CO;2-4

63. Gistelinck C, Kwon RY, Malfait F, Symoens S, Harris MP, Henke K, et al. Zebrafish type I collagen mutants faithfully recapitulate human type I collagenopathies. Proceedings of the National Academy of Sciences. 2018; 115(34):E8037–E8046. https://doi.org/10.1073/pnas.1722200115 PMID: 30082390

64. Newham E, Kague E, Aggleton JA, Fernee C, Brown KR, Hammond CL. Finite element and deformation analyses predict pattern of bone failure in loaded zebrafish spines. Journal of The Royal Society Interface. 2019; 16(160):20190430. https://doi.org/10.1098/rsif.2019.0430

65. Westneat MW. A biomechanical model for analysis of muscle force, power output and lower jaw motion in fishes. Journal of Theoretical Biology. 2003; 223(3):269–281. https://doi.org/10.1016/S0022-5193(03)00058-4

66. Tobias JH, Chow JW, Chambers TJ. Opposite effects of insulin-like growth factor-I on the formation of trabecular and cortical bone in adult female rats. Endocrinology. 1992; 131(5):2387–2392. https://doi.org/10.1210/endo.131.5.1425437

67. Goodyear SR, Gibson IR, Skakle JMS, Wells RPK, Aspden RM. A comparison of cortical and trabecular bone from C57 Black 6 mice using Raman spectroscopy. Bone. 2009; 44(5):899–907. https://doi.org/10.1016/j.bone.2009.01.008

68. Ott SM. Cortical or Trabecular Bone: What's the Difference? American Journal of Nephrology. 2018; 47(6):373–375.

69. Cadet ER, Gafni RI, McCarthy EF, McCray DR, Bacher JD, Barnes KM, et al. Mechanisms Responsible for Longitudinal Growth of the Cortex: Coalescence of Trabecular Bone into Cortical Bone. JBJS. 2003; 85(9). https://doi.org/10.2106/00004623-200309000-00013 PMID: 12954833

70. Mulder L, Koolstra JH, de Jonge HW, van Eijden TMGJ. Architecture and mineralization of developing cortical and trabecular bone of the mandible. Anatomy and Embryology. 2006; 211(1):71–78. https://doi.org/10.1007/s00429-005-0054-0

71. Altman AR, Tseng WJ, de Bakker CMJ, Chandra A, Lan S, Huh BK, et al. Quantification of skeletal growth, modeling, and remodeling by in vivo micro computed tomography. Bone. 2015; 81:370–379. https://doi.org/10.1016/j.bone.2015.07.037 PMID: 26254742

72. Tanck E, Hannink G, Ruimerman R, Buma P, Burger EH, Huiskes R. Cortical bone development under the growth plate is regulated by mechanical load transfer. Journal of Anatomy. 2006; 208(1):73–79. https://doi.org/10.1111/j.1469-7580.2006.00503.x

73. Doblarè M, García JM, Gómez MJ. Modelling bone tissue fracture and healing: a review. Engineering Fracture Mechanics. 2004; 71(13):1809–1840.

74. Kameo Y, Miya Y, Hayashi M, Nakashima T, Adachi T. In silico experiments of bone remodeling explore metabolic diseases and their drug treatment. Science Advances. 2020; 6(10). https://doi.org/10.1126/sciadv.aax0938 PMID: 32181336

75. Adachi T, Kameo Y, Hojo M. Trabecular bone remodelling simulation considering osteocytic response to fluid-induced shear stress. Philosophical Transactions of the Royal Society A: Mathematical, Physical and Engineering Sciences. 2010; 368(1920):2669–2682. https://doi.org/10.1098/rsta.2010.0073

76. Kameo Y, Adachi T. Interstitial fluid flow in canaliculi as a mechanical stimulus for cancellous bone remodeling: in silico validation. Biomechanics and Modeling in Mechanobiology. 2014; 13(4):851–860. https://doi.org/10.1007/s10237-013-0539-3

77. Carpenter RD, Carter DR. The mechanobiological effects of periosteal surface loads. Biomechanics and Modeling in Mechanobiology. 2008; 7(3):227–242. https://doi.org/10.1007/s10237-007-0087-9

78. Cowin SC, Gailani G, Benalla M. Hierarchical poroelasticity: movement of interstitial fluid between porosity levels in bones. Philosophical Transactions of the Royal Society A: Mathematical, Physical and Engineering Sciences. 2009; 367(1902):3401–3444. https://doi.org/10.1098/rsta.2009.0099

79. Fernández JR, García-Aznar JM, Martínez R. Piezoelectricity could predict sites of formation/resorption in bone remodelling and modelling. Journal of Theoretical Biology. 2012; 292:86–92. https://doi.org/10.1016/j.jtbi.2011.09.032

80. Sánchez MT, Pérez MÁ, García-Aznar J. The role of fluid flow on bone mechanobiology: mathematical modeling and simulation. Computational Geosciences. 2020.

81. Sfakiotakis M, Lane DM, Davies JBC. Review of fish swimming modes for aquatic locomotion. IEEE Journal of Oceanic Engineering. 1999; 24(2):237–252. https://doi.org/10.1109/48.757275

82. Bendsøe MP, Sigmund O. Topology Optimization. Springer-Verlag Berlin Heidelberg; 2004.

83. Pang H, Shiwalkar AP, Madormo CM, Taylor RE, Andriacchi TP, Kuhl E. Computational modeling of bone density profiles in response to gait: a subject-specific approach. Biomechanics and Modeling in Mechanobiology. 2012; 11(3):379–390. https://doi.org/10.1007/s10237-011-0318-y

84. Garijo N, Verdonschot N, Engelborghs K, García-Aznar JM, Pérez MA. Subject-specific musculoskeletal loading of the tibia: Computational load estimation. Journal of the Mechanical Behavior of Biomedical Materials. 2017; 65:334–343. https://doi.org/10.1016/j.jmbbm.2016.08.026

85. Voesenek CJ, Pieters RPM, van Leeuwen JL. Automated Reconstruction of Three-Dimensional Fish Motion, Forces, and Torques. PLOS ONE. 2016; 11(1):1–17. https://doi.org/10.1371/journal.pone.0146682

86. Voesenek CJ, Li G, Muijres FT, van Leeuwen JL. Experimental–numerical method for calculating bending moments in swimming fish shows that fish larvae control undulatory swimming with simple actuation. PLOS Biology. 2020; 18(7):1–24. https://doi.org/10.1371/journal.pbio.3000462

87. Molnar JL, Pierce SE, Hutchinson JR. An experimental and morphometric test of the relationship between vertebral morphology and joint stiffness in Nile crocodiles (Crocodylus niloticus). Journal of Experimental Biology. 2014; 217(5):758–768. https://doi.org/10.1242/jeb.089904

88. McCarty CA, Thomason JJ, Gordon KD, Burkhart TA, Milner JS, Holdsworth DW. Finite-Element Analysis of Bone Stresses on Primary Impact in a Large-Animal Model: The Distal End of the Equine Third Metacarpal. PLOS ONE. 2016; 11(7):1–22. https://doi.org/10.1371/journal.pone.0159541

89. Oliver JD, Jones KE, Hautier L, Loughry WJ, Pierce SE. Vertebral bending mechanics and xenarthrous morphology in the nine-banded armadillo (Dasypus novemcinctus). Journal of Experimental Biology. 2016; 219(19):2991–3002.

90. Wardle C, Videler J, Altringham J. Tuning in to fish swimming waves: body form, swimming mode and muscle function. Journal of Experimental Biology. 1995; 198(8):1629–1636. https://doi.org/10.1242/jeb.198.8.1629

91. Altringham JD, Ellerby DJ. Fish swimming: patterns in muscle function. Journal of Experimental Biology. 1999; 202(23):3397–3403. https://doi.org/10.1242/jeb.202.23.3397

92. Westneat MW, Wainwright SA. 7. Mechanical design for swimming: muscle, tendon, and bone. In: Tuna: Physiology, Ecology, and Evolution. vol. 19 of Fish Physiology. Academic Press; 2001. p. 271–311.

93. Katz SL. Design of heterothermic muscle in fish. Journal of Experimental Biology. 2002; 205(15):2251–2266. https://doi.org/10.1242/jeb.205.15.2251

94. Donley JM, Sepulveda CA, Konstantinidis P, Gemballa S, Shadwick RE. Convergent evolution in mechanical design of lamnid sharks and tunas. Nature. 2004; 429(6987):61–65. https://doi.org/10.1038/nature02435

95. Shadwick RE, Syme DA. Thunniform swimming: muscle dynamics and mechanical power production of aerobic fibres in yellowfin tuna (Thunnus albacares). Journal of Experimental Biology. 2008; 211(10):1603–1611. https://doi.org/10.1242/jeb.013250

96. Nakabo T. Fishes of Japan with pictorial keys to the species (3rd ed). Tokai University Press; 2013.